Journal of Materials Chemistry A



PAPER

View Article Online
View Journal | View Issue



Cite this: J. Mater. Chem. A, 2017, 5, 4036

Potential for high thermoelectric performance in n-type Zintl compounds: a case study of Ba doped KAlSb₄†

Brenden R. Ortiz,**a Prashun Gorai,**a Lakshmi Krishna,**a Rachel Mow,**c Armando Lopez,**a Robert McKinney,**a Vladan Stevanović**a and Eric S. Toberer**ab

High-throughput calculations (first-principles density functional theory and semi-empirical transport models) have the potential to guide the discovery of new thermoelectric materials. Herein we have computationally assessed the potential for thermoelectric performance of 145 complex Zintl pnictides. Of the 145 Zintl compounds assessed, 17% show promising n-type transport properties, compared with only 6% showing promising p-type transport. We predict that n-type Zintl compounds should exhibit high mobility μ_n while maintaining the low thermal conductivity κ_L typical of Zintl phases. Thus, not only do candidate n-type Zintls outnumber their p-type counterparts, but they may also exhibit improved thermoelectric performance. From the computational search, we have selected n-type KAlSb4 as a promising thermoelectric material. Synthesis and characterization of polycrystalline KAlSb4 reveals non-degenerate n-type transport. With Ba substitution, the carrier concentration is tuned between 10^{18} and 10^{19} e⁻ cm⁻³ with a maximum Ba solubility of 0.7% on the K site. High temperature transport measurements confirm a high μ_n (50 cm² V⁻¹ s⁻¹) coupled with a near minimum κ_L (0.5 W m⁻¹ K⁻¹) at 370 °C. Together, these properties yield a zT of 0.7 at 370 °C for the composition $K_{0.99}Ba_{0.01}AlSb_4$. Based on the theoretical predictions and subsequent experimental validation, we find significant motivation for the exploration of n-type thermoelectric performance in other Zintl pnictides.

Received 3rd November 2016 Accepted 23rd December 2016

DOI: 10.1039/c6ta09532a

www.rsc.org/MaterialsA

1 Introduction

The discovery of new materials with a high thermoelectric figure of merit zT remains a challenging and societally important problem within materials physics. 1-3 Historically, the search for new thermoelectric materials has been led by experiment with little knowledge of the underlying reciprocal space properties (e.g. electron and phonon band structures) due to the difficulty of accurately predicting the electronic and phonon transport entering zT.1,4-6 However, with the rise of high-throughput firstprinciples calculations, models for predicting transport properties and metrics for quantifying thermoelectric performance are beginning to emerge. Current high-throughput methods can be broadly classified into two categories: (i) those that determine charge carrier energies and velocities from calculations to predict performance within a Boltzmann transport model,7-12 and (ii) those that use semiempirical models that combine experimental data and first-principles calculations to predict performance. 13-15 Despite advances in computational throughput, the field has seen few experimental efforts that validate thermoelectric performance predictions or harness these searches to realize new classes of thermoelectric materials.

We have previously developed a metric for quantifying the potential for thermoelectric performance of materials. The metric is based on the quality factor β and can be evaluated directly from first-principles calculations and semi-empirical models in a computationally tractable, high-throughput fashion. Using β as the metric, we have performed a high-throughput search to identify promising families of materials.

Zintl pnictides, a historically successful class of p-type thermoelectric materials (e.g. Yb₁₄MnSb₁₁, ^{18,19} Sr₃GaSb₃, ²⁰ and Ca₅-Al₂Sb₆ ²¹), were one such family identified as having the potential for a high zT. However, contrary to the vast amount of experimental literature on p-type Zintl thermoelectrics, our computations find that n-type Zintl materials with high β are more numerous and have the potential to outperform their p-type counterparts. In this work, we employ a high-throughput search of 145 Zintl pnictides to investigate the differences in the intrinsic transport properties within Zintl compounds. We identify that n-type Zintls are an understudied, extremely promising class of materials. To validate our computational predictions we have selected KAlSb₄ as one of many promising n-type candidates.

aColorado School of Mines, Golden, CO, USA. E-mail: bortiz@mines.edu

^bNational Renewable Energy Laboratory, Golden, CO, USA

^{&#}x27;Harvey Mudd College, Claremont, CA, USA

[†] Electronic supplementary information (ESI) available. See DOI: 10.1039/c6ta09532a

P-type Zintl antimonides excel as thermoelectrics due to their extremely low lattice thermal conductivity; their critical weakness is often low charge carrier mobilities (<10 cm² V⁻¹ $\rm s^{-1}$). The predicted mobility of n-type KAlSb4 is quite high ($\sim\!100$ cm² V⁻¹ s⁻¹), suggesting that the conduction band edge states may enable improved charge transport without compromising the low lattice thermal conductivity typical of Zintl compounds. Interestingly, few Zintl compounds have been experimentally realized as n-type thermoelectric materials. The key exceptions are filled skutterudite and clathrate compounds. Both of these materials achieve n-type performance due to large guest sites that permit unusually flexible chemistry. Excluding skutterudite and clathrate structures, we have only identified Ba₅- $In_2Sb_6 (zT \sim 0.02)^{22}$ and $SrAl_2Si_2 (zT \sim 0.35)^{23}$ as materials with n-type performance. Several Mg-containing compounds have also been identified in the literature as n-type Zintl compounds $(Mg_3Sb_2^{24,25} \text{ and } Ba_{1.9}Ca_{2.4}Mg_{9.7}Si_7^{26})$. However, given the electropositive character of Mg, it is not clear that such compounds contain the requisite polyanionic framework to be considered traditional Zintl compounds.

Fig. 1 shows the crystal structure and extended bonding in KAlSb₄.27 The structure is charge balanced, with an infinite AlSb₄ polyanionic structure surrounding K⁺ ions. KAlSb₄ is comprised of infinite chains of corner-sharing AlSb₄ tetrahedra extending in the b-direction. Within the a-c directions, the AlSb₄ chains are interconnected by two varieties of Sb chains (denoted as (1) and (2) in Fig. 1). For each AlSb₄ tetrahedron, the connections are as follows:

- (1) Two Sb-chains consisting of trigonal pyramidal Sb groups extending in the b-direction.
- (2) One zig-zag chain of Sb extending in the *b*-direction. The total anionic framework created by the Al and Sb creates infinite channels of K atoms in the b-direction. The structure is reminiscent of BaGa2Sb2, which also contains channels of Ba atoms surrounded by an anionic framework of Ga-Sb. 28,29 Prior

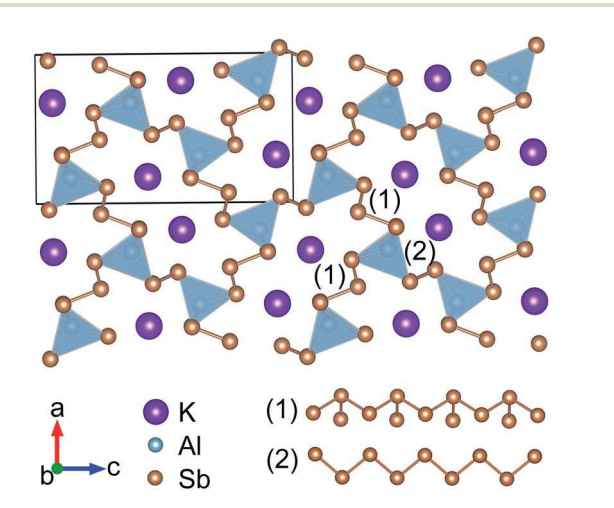


Fig. 1 Crystal structure of KAlSb₄ is comprised of infinite chains of corner-sharing AlSb₄ tetrahedra extending in the b-direction. The chains of AlSb₄ tetrahedra are interconnected by two chains of trigonal pyramidal Sb chain linkages (1) and one zig-zag Sb chain linkage (2). This structure creates infinite K-containing channels parallel to the b-direction.

work on KAlSb₄ is limited to the original structural study.²⁷ In that work, the compound was synthesized for the first time from the elements at 920 K.

Guided by our high-throughput search of Zintl pnictides, we report the synthesis and thermoelectric properties of $K_{1-r}Ba_r$ AlSb₄. The synthesis is conducted via high-energy ball milling followed by reactive uniaxial hot-pressing to yield dense, singlephase ingots. A combination of X-ray diffraction and carrier concentration measurements is utilized to determine the solubility limit of Ba in $K_{1-x}Ba_xAlSb_4$. High temperature resistivity, Hall effect, Seebeck coefficient, and thermal diffusivity measurements are used to reveal the electronic and thermal transport properties. Electronic structure calculations and analysis within the Boltzmann transport framework provide further insights into the underlying transport mechanisms. Overall $K_{1-x}Ba_xAlSb_4$ proves to be a promising thermoelectric material with a zT of 0.7 at 370 °C. For comparison, PbTe possesses a zT of 0.8 and 1.0 at 370 °C under optimal doping with iodine and lanthanum, respectively (this comparison does not include the extensive microstructural optimization PbTe has undergone in the last 30 years). 1,30 Our experimental work serves to validate the computational search and further encourages the exploration of n-type Zintls for a high zT.

2 Methods

Experimental

 $K_{1-x}Ba_xAlSb_4$ (0 $\leq x \leq 0.050$) is synthesized through highenergy ball milling followed by reactive uniaxial hot-pressing. All sample preparation, handling of powders, and measuring of raw reagents are performed in an argon dry box with oxygen concentration <1 ppm. We have empirically determined that the purest samples are obtained by adding elements according to $K_{1.00-x}Ba_xAl_{1.00}Sb_{3.80}$ to suppress the formation of Sb impurities. Elemental aluminum shot (Alfa 99.999%) is sectioned into small (<1 mm) pieces and loaded with antimony shot (Alfa 99.999%) and barium shavings taken from a barium rod (Alfa 99+%) into a tungsten carbide mill vial with two 7/16" tungsten carbide balls. Aluminum, barium, and antimony are ball milled for 60 min to pre-react aluminum and evenly disperse barium. Potassium is obtained by cutting deeply into potassium ingots (Alfa 99.5%) to reveal clean metal and then added directly to the Ba_xAlSb₄ mixture. The mixture is milled again for 15 cycles of duration 1 min. The vial is rotated between each cycle to prevent adhesion of powder to the walls of the vial. Powders are sieved through a 106 µm mesh adhering to ASTM E11 standards.

Polycrystalline ingots are formed via reactive hot pressing in a high-density graphite die under dynamic vacuum. The samples are heated to 500 °C within 3 h under 50 MPa of pressure. Densification occurs during a 500 °C soak for 15 h under 50 MPa. The samples then undergo stress-free annealing at 500 °C for 1 h, followed by controlled cooling to 50 °C in 1 h. The samples are sectioned into 1.5 mm thick discs and characterized. The sample densities were measured by a geometrical method and were consistently >97% of the density predicted by X-ray diffraction.

X-ray diffraction patterns are collected on a Bruker D2 Phaser diffractometer in a θ -2 θ configuration using Cu K α radiation. Refinement of the patterns utilized pure KAlSb₄ (ICSD: 300157) as the base pattern and the GSAS II software package.³¹ Refined parameters include lattice parameters, isotropic domain size, and atomic positions. Instrumental parameters are refined using a NIST LaB₆ sample to increase the fidelity of results. Energy dispersive spectroscopy (EDS) mapping of sample fracture surfaces is performed on a FEI Quanta 600i Scanning Electron Microscope (SEM).

Hall effect and resistivity measurements are performed using the Van der Pauw geometry on home-built apparatus. The measurements were conducted up to 400 °C under vacuum ($<10^{-4}$ Torr). Contacts are pressure-assisted nichrome wire. After the contacts are established, the samples are coated with boron nitride spray to suppress sublimation. A test sample was measured with and without the boron nitride coating; no change in the resistivity was observed as a result of the coating, but the high temperature stability under high vacuum was significantly improved. Seebeck coefficient measurements were conducted using the quasi-steady slope method at 400 °C under high vacuum ($<10^{-6}$ Torr). 32,33 The boron nitride coating is removed before Seebeck effect measurements are made.

The thermal diffusivity is measured using a Netzsch Laser Flash Apparatus (LFA) 457 and the resulting diffusivity data are fit using a Cowen plus Pulse Correction (CPC) numerical model. The samples are coated with graphite spray to reduce errors in the sample emissivity. The total thermal conductivity of the alloyed samples is calculated using

$$\kappa = D\rho C_{\rm p} \tag{1}$$

where D is the thermal diffusivity, ρ is the mass density, and $C_{\rm p}$ is the volumetric heat capacity. The heat capacity is estimated using the Dulong-Petit approximation.

Speed of sound measurements are performed using an Olympus 5072PR Pulser/Receiver system with a gain of 20 dB and a 5 kHz signal. Both longitudinal and shear measurements were made, using Olympus V112 (longitudinal) and Olympus V156 (shear) transducers and an Atten ADS 1102C oscilloscope.

2.2 Computational

Density functional theory (DFT) calculations were performed with the plane-wave basis VASP code, 34 with the exchange correlation functional in the Perdew–Burke–Ernzerhof (PBE) functional form within the projector augmented wave formalism. 35 For relaxing the structures of the 145 Zintl compounds (arsenides, antimonides, and bismuthides), a procedure similar to that described in ref. 13 and 36 was used with a plane-wave cutoff of 340 eV. A suitable on-site correction in the form of Hubbard U in the rotationally invariant form proposed by Dudarev *et al.* 37 was applied for transition metals following the methodology in ref. 38. The quality factor β is defined as

$$\beta = \frac{2e}{\hbar^3} \left(\frac{k_{\rm B}}{e}\right)^2 \left(\frac{k_{\rm B}}{2\pi}\right)^{3/2} \frac{\mu_0 m_{\rm DOS}^{*3/2}}{\kappa_L} T^{5/2} \tag{2}$$

where μ_0 is the intrinsic charge carrier mobility, m_{DOS}^* is the density of states (DOS) effective mass, κ_L is the lattice thermal conductivity, $k_{\rm B}$ is the Boltzmann constant, e is the electronic charge and \hbar is the reduced Planck constant. To address the challenges associated with the direct calculation of the transport properties, μ_0 and κ_L were calculated using semi-empirical models. To determine β , one needs to calculate the density of states effective mass m_{DOS}^* , the band effective mass m_{b}^* , and the bulk modulus B. The band effective mass m_b^* is evaluated from $m_{\rm DOS}^*$ and the band degeneracy $N_{\rm b}$, using the relationship $m_{\text{DOS}}^* = N_{\text{b}}^{2/3} m_{\text{b}}^*$ (assuming spherical and symmetric electron/ hole pockets). The band degeneracy N_b is determined from the electronic structure calculated on a dense k-point grid using our previously developed algorithm.13 The bulk modulus B is calculated by fitting the Birch-Murnaghan equation of state to a set of total energies computed at different volumes. The density of states effective mass m_{DOS}^* is determined from the DOS within the parabolic band approximation, such that the parabolic band reproduces the same number of states as the DOS within a 100 meV energy window from the relevant band edges.

For KAlSb₄, the electronic structure and the energy-decomposed charge densities are calculated on a dense k-point grid (6 \times 14 \times 4). The band effective masses $m_{\rm b}^*$ along the high symmetry paths of the orthorhombic Brillouin zone are calculated on a dense k-point grid by fitting a parabolic band ($\varepsilon = \pm \hbar^2 k^2 / 2m_{\rm b}^*$, where $\varepsilon = E - E_0$ and E_0 is the energy at the bottom/top of the band) to the band edges. Where the band edges significantly deviate from a parabolic band, a Kane dispersion model ($\varepsilon + \alpha \varepsilon^2 = \pm \hbar^2 k^2 / 2m_{\rm b}^*$, where α is the non-parabolicity factor) is used to obtain $m_{\rm b}^*$.

3 Results and discussion

3.1 Predicted properties of Zintl pnictides

First-principles calculations of the 145 Zintl arsenides, antimonides, and bismides were analyzed within the framework developed for β . ¹³ Compounds with $\beta > 10$ (roughly comparable to that of PbTe) were analyzed in aggregate to study general trends in transport properties that make the Zintl pnictides promising thermoelectric materials. Of the 145 compounds, 17% are predicted to have $\beta > 10$ for n-type transport whereas only 6% are predicted to have $\beta > 10$ for p-type transport. Please note that all calculations are available (alongside >2000 other materials) on https://www.tedesignlab.org.17 Furthermore, we find that the sources of large β are fundamentally different in Zintl compounds depending on the n or p-type transport. Fig. 2 provides a visualization of the average intrinsic transport properties of Zintl pnictides with $\beta > 10$ for n and p-type transport. For reference, the transport properties are compared with those of PbTe. All results used to produce Fig. 2 can be found in ESI, Table S1.† We note that there are many antimonides and bismuthides that do not explicitly appear in our data set due to the propensity of DFT to underestimate the band gap (vielding many antimonides and bismuthides as zero gap materials). However, we expect that many of the arsenide results will generalize to their antimonide and bismuthide analogues.

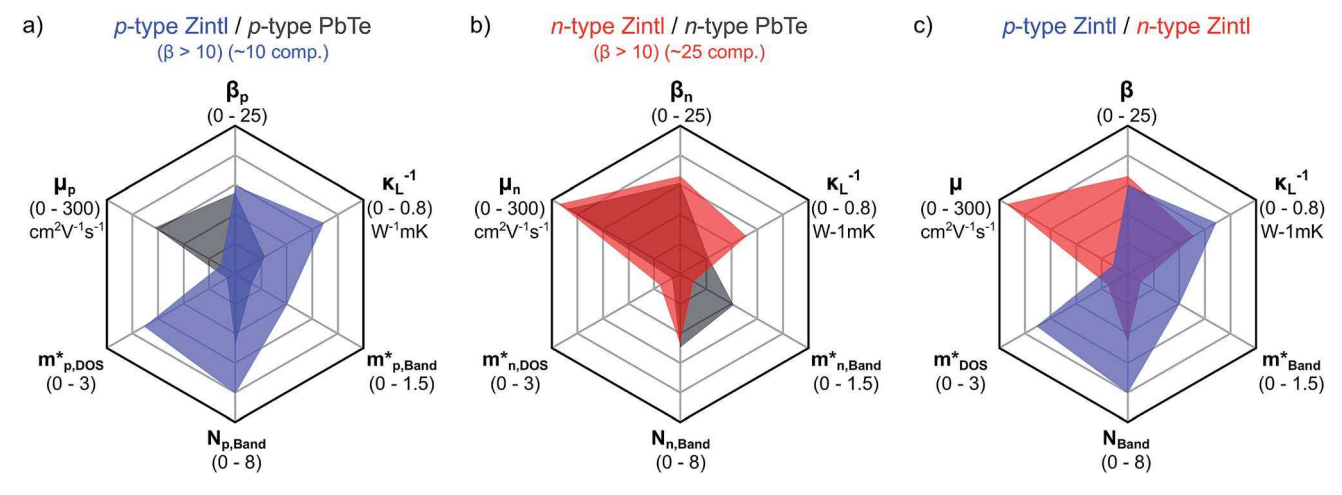


Fig. 2 Radar plots showing the average computed transport properties of p-type and n-type Zintl compounds ($\beta > 10$) with PbTe for comparison. The values for PbTe come from our calculations of β for the sake of self-consistency. (a) Comparison of a p-type Zintl with p-type PbTe, demonstrating that, on average, p-type Zintls have low hole mobility but exceptionally low thermal conductivity. Relatively few (8%) of the studied Zintls exhibit $\beta > 10$, due in part to the reduced hole mobility. (b) Comparison of a n-type Zintl with n-type PbTe, demonstrating that ntype Zintls have intrinsically high electron mobility, comparable to that of PbTe. The flexibility allowed to the other properties from the high mobility leads to a larger number of materials (17% of the studied Zintls) with $\beta > 10$. (c) Comparison of n-type and p-type Zintls, demonstrating the drastic difference between n and p-type Zintls. While both share similar β values, the intrinsically high mobility in n-type Zintls provides further means for optimization and less strict requirements on other transport properties.

In Fig. 2a, we find that p-type Zintl pnictides with $\beta > 10$ are characterized by lower hole mobilities, higher band degeneracies, and heavier effective masses compared to PbTe. These predictions are consistent with experimental results from wellknown p-type high zT Zintl compounds (e.g. Yb14MnSb11, 18,19 Ca₃AlSb₃,^{39,40} Sr₃GaSb₃,²⁰ and Ca₅Al₂Sb₆ (ref. 21)). Poor hole mobility requires a lower thermal conductivity to maintain β > 10, which is likely responsible for the relative scarcity of p-type Zintl pnictides with large β . Conversely, Fig. 2b demonstrates that the transport properties of n-type Zintl pnictides are comparable to those of n-type PbTe. The n-type Zintls possess high electron mobilities, low effective masses, and low thermal conductivity. Additionally, due to high electron mobility, the requirement for extremely low lattice thermal conductivity is relaxed; consequently, the number of n-type Zintl candidates is larger than the p-type candidates. Fig. 2c directly compares the average properties of the p and n-type Zintl pnictides. While both p and n-type Zintls have comparable average β , we see that the underlying transport properties are drastically different. The performance of p-type Zintls is driven by extremely low thermal conductivity, whereas n-type Zintls boast both high electron mobility and low thermal conductivity. The larger number of n-type Zintls with high β combined with the intrinsically high electron mobility strongly motivates further experimental work on the n-type Zintl family. This is in stark contrast with the vast majority of the Zintl literature, which is almost exclusively p-type.

3.2 KAlSb₄ structure and composition

To test the validity of these calculations for n-type Zintl compounds, KAlSb4 is explored experimentally. Our synthesis procedure yields dense (>97% theoretical density) discs of KAlSb₄. The crystal structure and phase purity of sintered $K_{1-x}Ba_xAlSb_4$ samples were assessed by X-ray diffraction (XRD) and subsequent Rietveld refinement. Fig. 3 shows a typical XRD diffraction pattern collected on pure KAlSb₄. Additional XRD results can be found in ESI, Fig. S1.† For all hot-pressed samples, we identify a small (1-2 vol%) impurity phase which cannot be indexed by XRD. Additionally, for Ba-containing samples with Ba concentration $x \ge 0.01$, an additional impurity

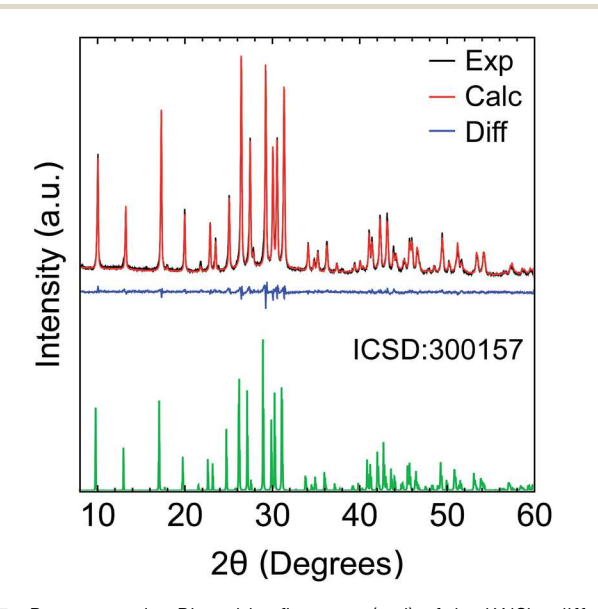


Fig. 3 Representative Rietveld refinement (red) of the KAlSb₄ diffraction pattern (black) and associated difference profile (blue). ICSD diffraction pattern 300157 of KAISb4 is shown for comparison. Rietveld results indicate that the material is phase pure KAlSb₄ and yields a reduced $\chi^2 \sim 2.5$.

phase appears. However, due to possible peak overlap with KAlSb₄ and the weak diffraction intensity of the secondary phase, it also cannot be indexed. The appearance of the impurity phase with increasing Ba content suggests the termination of solid-solubility around x = 0.010. However, due to the similar ionic radii of Ba²⁺ and K⁺ and generally low concentration of Ba, no trend is observed in the lattice parameters or cell volume. Energy dispersive spectroscopy (EDS) confirms that the average composition of the samples is consistent with the KAlSb₄ crystal structure, within the error of EDS. EDS finds that the primary impurity phase (1-2 vol%) is an Al-rich K-poor phase, consistent with AlSb (which we have observed as a common contaminant in the KAlSb₄ system).

3.3 Electronic properties

Unlike many charge-balanced Zintl compounds commonly studied in the thermoelectric community, KAlSb₄ is intrinsically n-type at room temperature. We note that the samples of KAlSb₄ synthesized with different impurities (e.g. AlSb and Sb) are also n-type. Ba-Doping successfully increases the electron concentration, consistent with Bak substitutional defects. Fig. 4 demonstrates the trend in carrier concentration as a function of nominal doping concentration at 250 °C.

As suggested by the evolution of a secondary phase in XRD, the effectiveness of Ba as a dopant in KAlSb₄ appears to plateau around x = 0.010. Assuming a linear relationship between the electron concentration and the Ba content, we extrapolate that the solubility of Ba in KAlSb₄ is approximately $x \sim 0.007$. Assuming that each Ba_K yields one free electron, the expected doping efficiency of Ba in KAlSb₄ is approximately 50%. This is consistent with the relatively low doping efficiency observed in

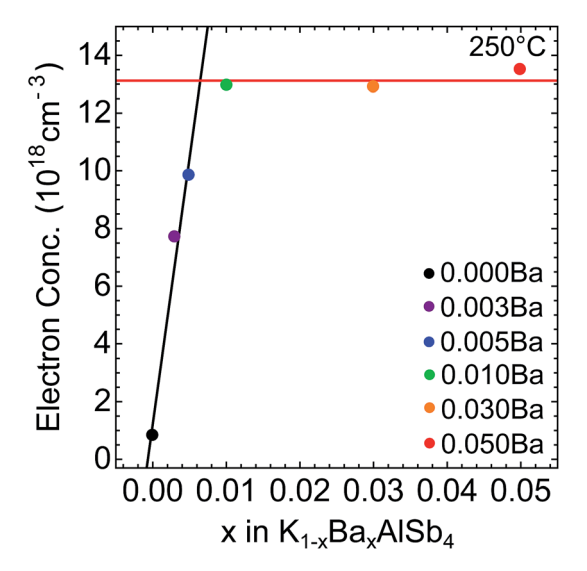


Fig. 4 Trend of electron carrier concentration with nominal dopant concentration is roughly linear up to the solubility limit of Ba. We find that the dopant effectiveness of Ba is approximately 50% of that expected of a perfect substitutional defect Ba_K⁺ yielding one free electron per Ba atom. Solubility limit of Ba is extrapolated to be $x \sim 0.007$, which is consistent with the appearance of a secondary phase in samples containing $x \ge 0.010$ Ba. Note that the plot is constructed at 250 °C; however, the qualitative results are identical for all temperatures.

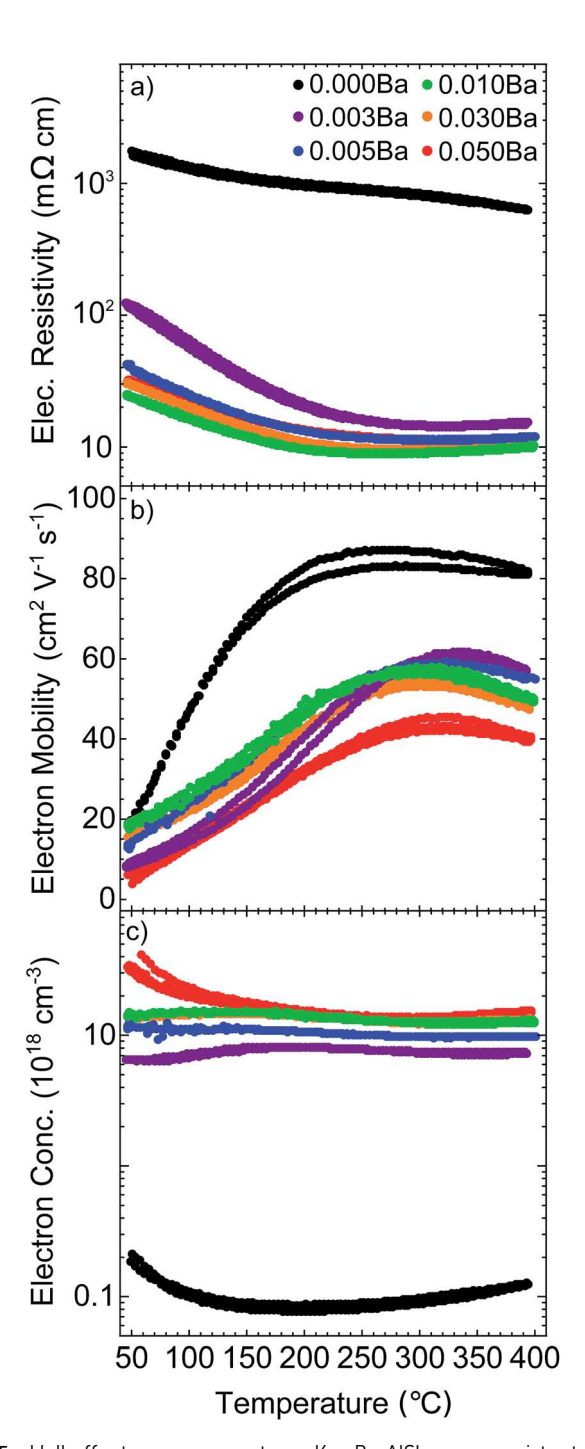


Fig. 5 Hall effect measurements on $K_{1-x}Ba_xAlSb_4$ are consistent with the n-type doping of an intrinsic semiconductor. Measurements on undoped KAlSb₄ (black) yield high resistivity (a), high mobility (b), and low n-type carrier concentration (c). With Ba doping, the mobility and resistivity decrease, consistent with increased charged impurity scattering. Carrier concentration increases with Ba doping up to the solubility limit of Ba (\sim 0.7%). In all samples, the mobility and resistivity exhibit strong temperature dependence at low temperatures (<250 °C). Due to the temperature invariance of the carrier concentration, we conclude that the temperature dependence at low temperatures is likely a combination of grain boundary oxidation and contact resistance.

chemically related Zintl compounds such as Zn-doped Ca₃-AlSb₄, Na-doped Ca₅Al₂Sb₆ and Zn-doped Sr₃GaSb₃, ^{20,21,40}

Successful doping of KAlSb₄ with Ba at concentrations $x \le$ 0.010 yields decreases in the electrical resistivity and electron mobility consistent with n-type doping. Fig. 5 shows the temperature dependence of the electronic resistivity, mobility, and carrier concentration for the samples of $K_{1-x}Ba_xAlSb_4$. The electrical resistivity (Fig. 5a) decreases monotonically up to the solubility of Ba (x = 0.010), consistent with doping via Ba_K. The electrical resistivity and electron mobility in KAlSb₄ are strongly temperature dependent from 50 °C to 250 °C. The temperature dependence cannot be ascribed to carrier activation, however, as the carrier concentration is largely temperature independent for doped samples (Fig. 5c). Similar activated behavior has been observed in the samples of Ca₃AlSb₃, Sr₃AlSb₃, and Sr₃GaSb₃ and has been attributed to oxidation at grain boundaries. 20,39-41

We also see strong evidence that the increased resistivity at low temperatures is, at least partially, due to contact resistance with the Van der Pauw leads. Changes in lead metal (copper, tungsten, nichrome, etc.) have no effect on the resistivity, but repeated annealing of the contact consistently yields reductions in the 'activated behavior' observed in the samples of KAlSb₄ at low to moderate temperatures. We note that replacing the contacts requires another annealing cycle to recover the reduced resistivity, consistent with a contact annealing process. During repeated cycling, we observe no change in the high temperature transport. The activated character of the resistivity and mobility is never eliminated completely and is likely a combination of the contact resistance and grain boundary

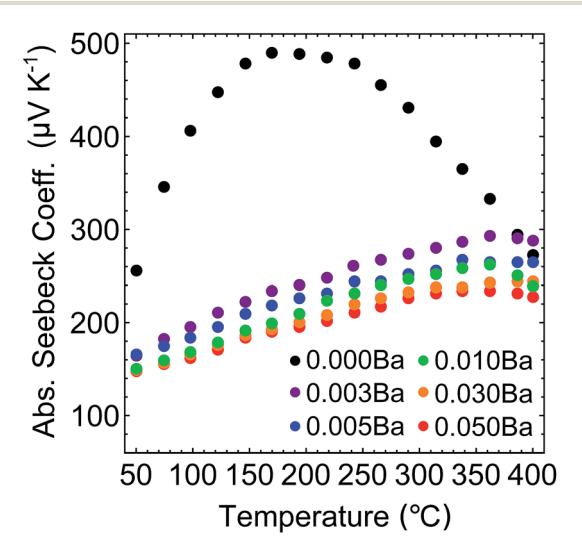


Fig. 6 Seebeck coefficient measurements on K_{1-x}Ba_xAlSb₄ are consistent with n-type doping of a nominally intrinsic semiconductor. Intrinsic KAlSb₄ (black) demonstrates a high Seebeck coefficient which peaks at $-495~\mu V~K^{-1}$ at approximately 170 °C before thermally induced bipolar transport reduces the Seebeck coefficient at high temperatures. From the peak of the Seebeck coefficient, we estimate the thermal band gap of KAlSb₄ to be approximately 0.5 eV. For samples containing $x \ge 0.010$ Ba, the Seebeck coefficient continues to fall, despite the carrier concentration remaining constant. Further reductions in the Seebeck coefficient beyond this point are attributed to the deleterious effect of the secondary phase.

oxidation. By ~250 °C, the activated character is largely eliminated. To reduce uncertainty in any comparisons done with Hall effect measurements (e.g. Pisarenko), the comparisons are done at 250 °C.

Fig. 6 shows the temperature dependent Seebeck coefficient of the samples of K_{1-r}Ba_rAlSb₄. Seebeck measurements on K_{1-x}Ba_xAlSb₄ are negative, consistent with the Hall effect measurements and the introduction of Ba_K defects via doping. The Seebeck coefficient of the doped samples decreases with increasing Ba concentration, as expected for a moderately doped semiconductor. We note that the Seebeck coefficient continues to decay for the samples beyond the solubility limit of Ba. We attribute the decrease to the deleterious effect of the secondary phase, as the carrier concentration for all samples above x = 0.010 is largely constant (Fig. 5c).

We see a significant bipolar contribution in undoped KAlSb₄. The Seebeck coefficient peaks at $-495 \,\mu\text{V K}^{-1}$ at 200 °C. From the peak of the Seebeck coefficient, we estimate the thermal band gap of KAlSb₄ to be approximately 0.5 eV.⁴² All doped samples exhibit near linearly rising Seebeck coefficients, consistent with the behavior of a moderately doped semiconductor.

Fig. 7 illustrates the effect of doping on the Seebeck coefficient measured at 250 °C. Consistent with Ba-doping, the Seebeck coefficients are negative and decrease with increasing electron concentration. We model the effect of doping on the Seebeck coefficient in KAlSb4 by solving the Boltzmann transport equation (BTE) within the relaxation time approximation for the Seebeck coefficient S as a function of the reduced chemical potential η (eqn (3)). For ease of comparison with other thermoelectric work, we assume that the system adheres

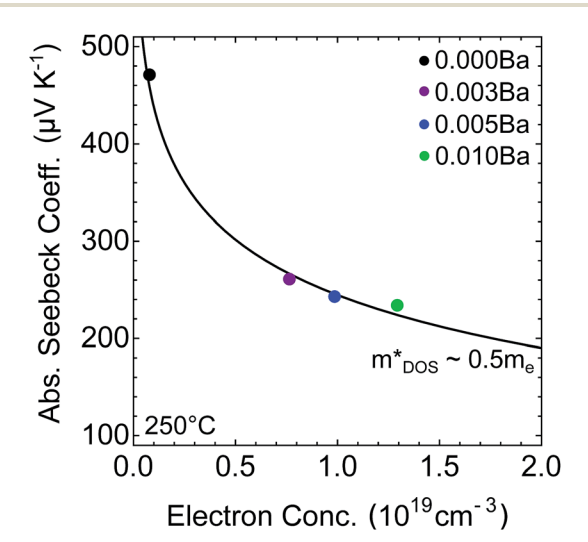


Fig. 7 Pisarenko plot of $K_{1-x}Ba_xAlSb_4$ generated using the single parabolic band (SPB) model to fit experimental data with the effective mass m_{DOS}^* as the only free parameter. For $K_{1-x}Ba_xAlSb_4$ we obtain $m_{\rm DOS}^* \sim 0.5 m_{\rm e}$. The Pisarenko plot is constructed at 250 °C; however, we note that the effective mass obtained from the data is unchanged for measurements at other temperatures. The undoped sample (black) is not explicitly included in the mathematical fit, as the effect of bipolar transport makes the temperature dependence unreliable for a Pisarenko fit. Samples with $x \ge 0.010$ are not included due to the presence of the secondary phase.

to the single parabolic band (SPB) model. However, due to the quasi-2D nature of the band structure surrounding Γ , care must be taken when drawing conclusions from the SPB model. By performing calculations at elevated temperatures (≥ 250 °C), we assume that acoustic phonon scattering is the dominant scattering mechanism (allowing $\lambda=0$). The full form of the Fermi integral $F(\eta)$ is given by eqn (4) where ξ is the reduced carrier energy.⁴³

$$S(\eta) = \frac{k_{\rm B}}{e} \frac{(2+\lambda)F_{1+\lambda}(\eta)}{(1+\lambda)F_{2}(\eta)} - \eta \tag{3}$$

$$F_{1+\lambda}(\eta) = \int_0^\infty \frac{\xi^{1+\lambda}}{1 + e^{\xi - \eta}} d\xi \tag{4}$$

We can now define the carrier concentration as a function of the reduced chemical potential and the density of states (DOS) effective mass m_{DOS}^* (eqn (5)):

$$n = 4\pi \left(\frac{2m_{\text{DOS}}^* k_{\text{B}} T}{h^2}\right)^{3/2} F_{1/2}(\eta)$$
 (5)

where n is the carrier concentration, T is the temperature, $k_{\rm B}$ is the Boltzmann constant, and h is the Planck constant.

From eqn (3) and (4) we can generate a hypothetical Seebeck coefficient S as a function of the chemical potential η . Substitution of eqn (5) further allows us to write the Seebeck coefficient as a function of the carrier concentration and the DOS effective mass. The resulting expression is fit to the experimental data in Fig. 7 to determine the DOS effective mass. We find that electrons in KAlSb₄ have an approximate DOS mass of $0.5m_{\rm e}$. We obtain similar results for calculations and fits performed at 150 °C, 250 °C, and 350 °C. Note that the point at x=0.000 Ba is not explicitly included in the fitting as the temperature dependent Seebeck measurements (Fig. 6) indicate a significant contribution from bipolar effects.

3.4 Thermal transport

The thermal diffusivity of KAlSb₄ was measured up to 400 °C. The total thermal conductivity can be found in ESI, Fig. S2 † as a function of temperature and doping concentration. The total thermal conductivity is a combination of the lattice, electronic, and bipolar contributions to the thermal conductivity. To decouple the electronic contribution to the thermal conductivity from the lattice and bipolar contributions, the Wiedemann–Franz relationship $\kappa_{\rm e}=LT/\rho$ is used to estimate the electronic contribution to the thermal conductivity. The Lorenz number L is calculated within the SPB model according to eqn (6).⁴³

$$L = \left(\frac{k_{\rm B}}{e}\right)^2 \frac{(1+\lambda)(3+\lambda)F_{\lambda}(\eta)F_{\lambda+2}(\eta) - (2+\lambda)^2 F_{\lambda+1}(\eta)^2}{(1+\lambda)^2 F_{\lambda}(\eta)^2}$$
 (6)

where the reduced chemical potential η is calculated from the experimentally observed Seebeck coefficients according to eqn (3). Again we assume that scattering is dominated by acoustic phonon scattering ($\lambda=0$). However, we acknowledge that the low temperature electronic transport has significant

contributions from the activated transport which will increase error in the calculation of the lattice thermal conductivity at low temperatures. The calculated Lorenz numbers for all samples can be found in ESI, Fig. S3.† We find that the electronic contribution to the thermal conductivity is relatively low (\leq 0.1 W m⁻¹ K⁻¹) for most temperatures and compositions. Subtracting the electronic contribution to the thermal conductivity results in the curves seen in Fig. 8. Only the undoped sample demonstrates a significant bipolar contribution at temperatures >200 °C. Due to the low concentration of Ba and the similarity of the Ba and K ionic radii, we see little to no change in the lattice thermal conductivity as a function of Ba concentration.

We can apply the Debye–Callaway model to fit the lattice thermal conductivity in KAlSb₄ as a function of temperature. We assume that the total thermal conductivity is composed of two terms, the contributions from acoustic phonons κ_a and the contribution from optical phonons κ_o . Under the high-temperature limit for the Debye–Callaway spectral heat capacity, and assuming only Umklapp scattering plays a significant role in the scattering of phonons, the acoustic component of the lattice thermal conductivity reduces to eqn (7).⁴⁴

$$\kappa_{\rm a} = \frac{(6\pi^2)^{2/3}}{4\pi^2} \left(\frac{M\nu_{\rm g}^3}{TV^{2/3}\gamma^2} \right) \left(\frac{1}{N^{1/3}} \right) \tag{7}$$

where M is the average mass (per atom), ν_g is the phonon group velocity, γ is the Gruneisen parameter, V is the average volume (per atom), and N is the number of atoms in the primitive cell.

For the optical mode contribution to the lattice thermal conductivity, we assume that the optical modes exhibit a glass-like conductivity. Again assuming the high temperature limit of the spectral heat capacity, we obtain the temperature independent glassy limit, eqn (8).⁴⁴

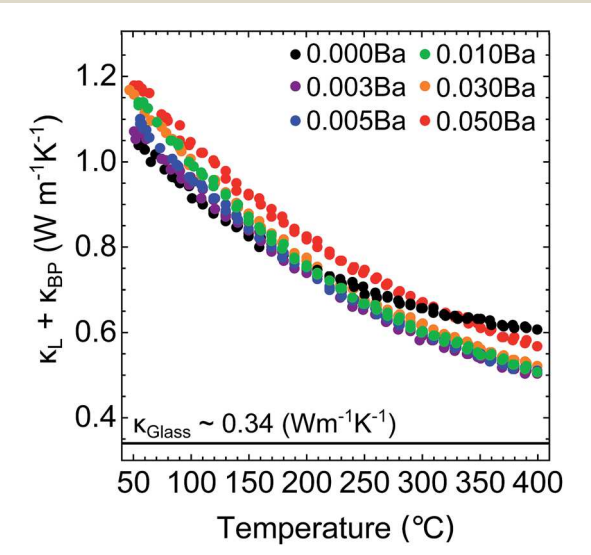


Fig. 8 The lattice thermal conductivity in doped samples is largely unchanged with respect to Ba concentration. Intrinsic KAlSb₄ exhibits a strong bipolar contribution beyond 200 °C, consistent with an undoped, small-gap semiconductor. Due to relatively high electrical resistivity, the subtracted electronic contribution to the thermal conductivity is only $\sim\!0.1$ W m $^{-1}$ K $^{-1}$.

$$\kappa_{\rm o} = \frac{3k_{\rm B}\nu_{\rm g}}{2V^{2/3}} \left(\frac{\pi}{6}\right)^{1/3} \left(1 - \frac{1}{N^{2/3}}\right) \tag{8}$$

where $k_{\rm B}$ is the Boltzmann constant. We approximate the phonon group velocity $\nu_{\rm g}$ by the average speed of sound ($\nu_{\rm g}(\omega) \sim$ v_s). Ultrasonic measurements performed on KAlSb₄ show that $\nu_{Trans} \sim 3230 \text{ m s}^{-1}$ and $\nu_{Shear} \sim 1900 \text{ m s}^{-1}$, which yields an average speed of sound of $v_s \sim 2350 \text{ m s}^{-1}$. The speed of sound in KAlSb4 is consistent with those of chemically similar Zintl compounds like Ca₅Al₂Sb₆, Sr₃GaSb₃, Sr₃AlSb₃, and Ca₃-AlSb₃.^{20,21,39,41} For KAlSb₄, we find the glassy contribution from optical modes to be \sim 0.34 W m⁻¹ K⁻¹.

We fit the sum of the acoustic (eqn (7)) and optical (eqn (8)) contributions to the lattice thermal conductivity for the sample containing x = 0.01Ba (ESI, Fig. S4†). The calculated fit utilizes γ \sim 3. We note that the thermal transport near room temperature exhibits a stronger temperature dependence than that predicted by the Debye-Callaway model. At high temperatures, however, the data are observed to roughly follow a T^{-1} dependence (consistent with phonon-phonon dominated scattering). In the calculation of the Lorenz number and the electronic contribution to thermal conductivity, we assumed that scattering is dominated by acoustic phonon scattering ($\lambda = 0$). However, it is evident in the electrical resistivity and electron mobility (Fig. 5) that the electronic transport at temperatures <250 °C is not entirely dominated by acoustic phonon scattering. Thus, we expect the low temperature Lorenz number and electronic correction to the thermal conductivity to be less accurate than the high temperature correction. This could contribute to the deviation in the Debye-Callaway fit at low temperatures.

3.5 Figure of merit

The figure of merit zT of $K_{1-x}Ba_xAlSb_4$ is shown in Fig. 9. We find that a maximum zT value of 0.7 is obtained at 370 °C for the

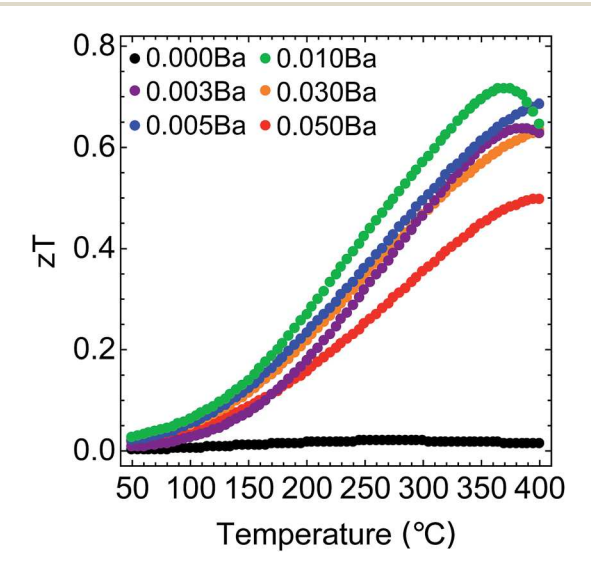


Fig. 9 We find that $K_{0.990}Ba_{0.010}AlSb_4$ exhibits a peak zT of 0.7 at 370 °C. Consistent with carrier concentration optimization, the peak zT rises with doping up to the solubility limit of Ba. All samples with $x \ge z$ 0.010 exhibit a reduced zT due to deleterious effects of the secondary phase

nominal composition $K_{0.990}Ba_{0.010}AlSb_4$. The peak zT in the samples of KAlSb₄ generally increases with Ba-doping until the solubility of Ba is reached at x = 0.010. Further addition of Ba after this point causes secondary phase formation that is deleterious to the Seebeck coefficient, electrical resistivity, thermal conductivity, and thus zT.

The SPB model can be used to evaluate the zT of a particular material as a function of the reduced chemical potential given the experimental mobility, density of states effective mass, lattice thermal conductivity, and temperature. The predicted zTvalues of KAlSb₄ as a function of carrier concentration at 370 °C are shown in ESI, Fig. S5†. The experimental data points for phase-pure samples are overlaid on ESI, Fig. S5† to evaluate the accuracy of the prediction. We see that the experimental samples are well represented by the model. Furthermore, the doping levels obtained in the x = 0.010 sample are approximately equal to the predicted optimal doping level, although further optimization may allow a zT > 0.8.

3.6 Electronic structure calculations

Electronic structure calculations were performed on KAlSb₄ to provide further insight into the fundamental electronic properties. The calculated band structure of KAlSb4 is shown in Fig. 10. KAlSb₄ has a direct gap (\sim 0.2 eV) at the Γ point and an additional low-lying conduction band at $Z_1 \sim 20$ meV above the conduction band edge. The DFT estimated bandgap (\sim 0.20 eV) agrees well with the thermal bandgap estimated from the Seebeck coefficient measurements (~ 0.5 eV), considering the propensity of DFT to underestimate the bandgap.

Both the conduction and valence bands exhibit significant anisotropy in the band effective masses (m_h^*) . The conduction band forming the band edge is highly dispersive (low effective mass and high velocity) along Γ -X and Γ -Y directions in the

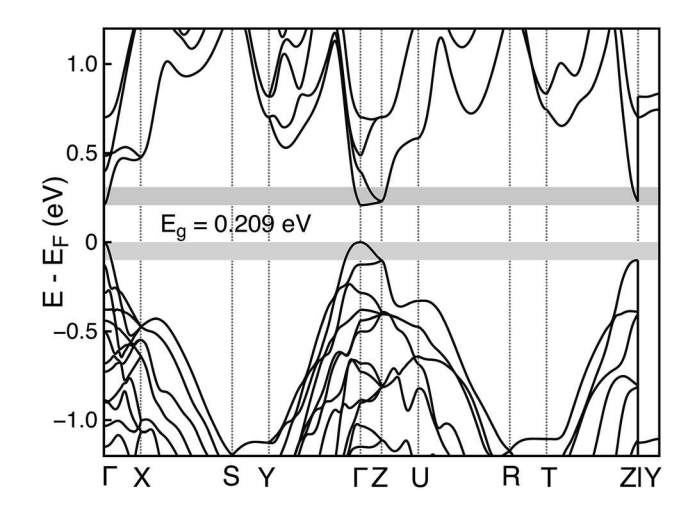


Fig. 10 Calculated band structure of KAlSb₄. The shaded regions denote 100 meV energy windows from the corresponding band edges. Calculations confirm that KAISb4 is a small-gap semiconductor. The conduction band effective masses along Γ -X and Γ -Y are small while Γ –Z is significantly larger. A second, isotropic, more dispersive conduction band converges well within the 100 meV window, and may play a role in maintaining high mobility in the n-type material.

	Γ-X	Γ – Y	Γ – Z	<i>Z</i> – <i>T</i>	Z-U	<i>Z</i> –Γ
$m^*_{ m b,CB} \ m^*_{ m b,VB}$	0.07 0.13	0.09 0.64	5.11 0.70	0.09	0.07	0.02

Brillouin zone. However, in the Γ –Z direction, the same band is significantly heavier. We observe the presence of a second band at the Z-point which is highly dispersive and significantly more isotropic (see Table 1). Due to the energetic proximity of the band at Z (\sim 20 meV off the true conduction band edge) and the polycrystalline nature of the samples studied here, the secondary band likely plays a role in maintaining high charge carrier mobility in n-type KAlSb4. Conversely, the band corresponding to the valence band edge is relatively heavy along Γ –X and Γ –Z directions but much more dispersive along Γ –X. A second band that converges to within 106 meV from the valence band edge is almost flat (non-dispersive) along Γ –Z.

To investigate the orbital contributions to the band edge states, we calculated the atom-projected DOS (see ESI, Fig. S6†). The conduction band edge is primarily composed of states derived from Sb p and s orbitals while the valence band edge is dominated by the contribution from Sb p orbitals. While relative contributions to the DOS from the antimony and aluminum atoms are expected to be accurate, it is not clear if a simple decomposition to p and s orbitals is applicable in Zintl compounds where significant hybridization of orbitals may occur.

Fig. 11 shows the charge density derived from electronic states that lie within 30 meV of the valence and conduction band edges. Both the valence and conduction band edges are dominated by Sb states, consistent with the atom-projected DOS (ESI, Fig. S6†). Aluminum and potassium contribute negligibly to the atomic states at the conduction and valence band edges.

The shape of the charge density isosurface in the valence band (Fig. 11a) is suggestive of lone pairs that extend towards the cationic channels of potassium. However, not all Sb atoms contribute to the valence band edge states since the charge density is primarily concentrated on Sb atoms that form trigonal pyramidal chains (Fig. 11b). In the conduction band, the charge density is associated with both the trigonal pyramidal and zig-zag chains of antimony (Fig. 11c and d). However, the bonds appear to exhibit nodes, characteristic of Sb-Sb antibonding states. While both the valence and conduction band edge states are derived from Sb orbitals, the valence band is dominated by Sb lone pair states, whereas, the conduction band is composed of anti-bonding states along the polyanionic framework. These interpretations are consistent with simple molecular orbital arguments and the calculated atom-projected DOS (ESI, Fig. S6†).

Both the pDOS and electron density isosurfaces indicate that the conduction band is strongly determined by antimony states. As such, these calculations highlight opportunities for enhancing the thermoelectric properties of n-type KAlSb₄. Alloying on either the potassium or aluminum sites may enable tuning of other transport properties while leaving the intrinsically high n-type mobility of KAlSb₄ unaffected.

4 Conclusion

Our high-throughput computational search reveals that n-type Zintl compounds with high β outnumber and possibly outperform their p-type counterparts. Furthermore, we find that n-type Zintls should possess high electron mobility while maintaining the low lattice thermal conductivity characteristic of Zintl compounds. These results inspired us to consider the n-type Zintl compound KAlSb₄ doped with Ba. A combination of XRD and Hall effect measurements yielded a solubility of Ba of 0.7%, which corresponds to a doping level of approximately 2 × 10^{19} e⁻ cm⁻³. Combined with the extremely low lattice thermal conductivity (\sim 0.5 W m⁻¹ K⁻¹ at 370 °C), the relatively high electron mobility (50 cm² V⁻¹ s⁻¹) yields a peak zT of 0.7 at

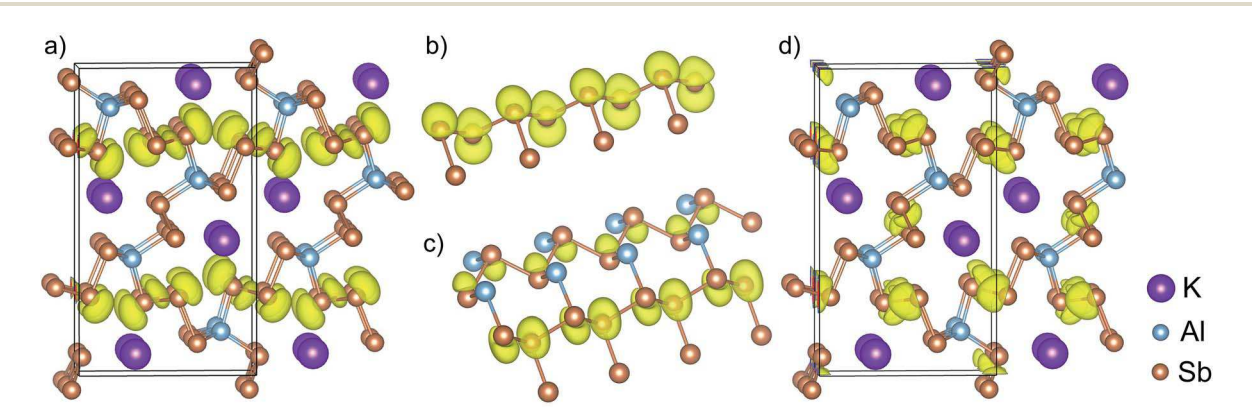


Fig. 11 Charge density isosurfaces of the electronic states that lie within 30 meV of both the valence (a and b) and conduction (c and d) band edges. We note that both conduction and valence band edges are dominated by Sb-derived states. The valence band is comprised of lone pairs, which are concentrated on the trigonal pyramidal chains and oriented towards the cationic potassium channels. The conduction band consists of anti-bonding states spread along both the trigonal pyramidal and zig-zag chains of Sb.

370 °C. Further, these results begin to validate our semiempirical β model as an effective search strategy.

Our calculations of the electronic structure of KAlSb₄ reveal that the material is a small-gap semiconductor with valence and conduction band edge states dominated by antimony states. Band masses on the conduction band edge (Γ point) are heavily anisotropic, characterized by a mix of extremely light masses $(0.07m_e$ and $0.09m_e$) and a heavy mass $(5.11m_e)$. The presence of a light, secondary, and more isotropic band at Z only 20 meV above the primary band edge likely plays a role in maintaining high mobility in KAlSb₄.

Computationally guided material development has the potential to revolutionize materials science and hasten the development and commercialization of new materials. This work begins to lay the foundation for an unstudied class of thermoelectric materials: n-type complex Zintl phases. Despite plentiful work on p-type Zintls, this work is one of the few reports on the thermoelectric properties of an n-type Zintl. Additionally, our work demonstrates the potential for a high zTin many other n-type Zintls. Coupled with the fact that almost twice as many n-type Zintls are predicted to be good thermoelectrics (when compared to p-type Zintls), we stress that further effort should be directed towards the characterization and synthesis of n-type Zintl compounds.

Acknowledgements

We acknowledge support from the National Science Foundation under the NSF DMR-1334713. The use of high performance computing resources of NREL's Computational Science Center is gratefully acknowledged. Rachel Mow was supported under a Research Experience for Undergraduates (REU) program through the National Science Foundation, award NSF DMR-1461275, REU Site: Research Experiences for Undergraduates in Renewable Energy.

References

- 1 G. J. Snyder and E. S. Toberer, Nat. Mater., 2008, 105-114.
- 2 L. Bell, Science, 2008, 321, 1457-1461.
- 3 L. Baranowski, G. J. Snyder and E. S. Toberer, Energy Environ. Sci., 2012, 5, 9055.
- 4 C. J. Vineis, A. Shakouri, A. Majumdar and M. G. Kanatzidis, Adv. Mater., 2010, 3970-3980.
- 5 A. J. Minnich, M. S. Dresselhaus, Z. F. Ren and G. Chen, Energy Environ. Sci., 2009, 466-479.
- 6 S. Curtarolo, G. L. Hart, M. B. Nardelli, N. Mingo, S. Sanvito and O. Levy, Nat. Mater., 2013, 191-201.
- 7 G. K. H. Madsen, J. Am. Chem. Soc., 2006, 128, 12140-12146.
- 8 J. Carrete, N. Mingo, S. Wang and S. Curtarolo, Adv. Funct. Mater., 2014, 24, 7427-7432.
- 9 Y. Zhang, E. Skoug, J. Cain, V. Ozolins, D. Morelli and C. Wolverton, Phys. Rev. B: Condens. Matter Mater. Phys., 2012, 85, 054306.
- 10 I. Opahle, A. Parma, E. J. McEniry, R. Drautz and G. K. H. Madsen, New J. Phys., 2013, 15, 105010.

- 11 I. Opahle, G. K. H. Madsen and R. Drautz, Phys. Chem. Chem. Phys., 2012, 14, 16197.
- 12 H. Zhu, G. Hautier, U. Aydemir, Z. M. Gibbs, G. Li, S. Bajaj, J.-H. Pohls, D. Broberg, W. Chen, A. Jain, M. A. White, M. Asta, G. J. Snyder, K. Persson and G. Ceder, J. Mater. Chem. C, 2015, 3, 10554.
- 13 J. Yan, P. Gorai, B. R. Ortiz, S. Miller, S. A. Barnett, T. Mason, V. Stevanovic and E. S. Toberer, Energy Environ. Sci., 2015, 983-994.
- 14 S. Wang, Z. Wang, W. Setyawan, N. Mingo and S. Curtarolo, Phys. Rev., 2006, 128, 021012.
- 15 P. Gorai, P. Parilla, E. S. Toberer and V. Stevanović, Chem. Mater., 2015, 27, 6213.
- 16 R. Chasmar and R. Stratton, The thermoelectric figure of merit and its relation to thermoelectric generators, J. Electron. Control, 1959, 7, 52-72.
- 17 P. Gorai, D. Gao, B. Ortiz, S. Miller, S. A. Barnett, T. Mason, Q. Lv, V. Stevanović and E. S. Toberer, Comput. Mater. Sci., 2016, 112, 368-376.
- 18 E. S. Toberer, S. R. Brown, T. Ikeda, S. M. Kauzlarich and J. G. Snyder, Appl. Phys. Lett., 2008, 062110.
- 19 E. S. Toberer, C. A. Cox, S. R. Brown, T. Ikeda, A. F. May, S. M. Kauzlarich and G. J. Snyder, Adv. Funct. Mater., 2008, 2795-2800.
- 20 A. Zevalkink, W. G. Zeier, G. Pomrehn, W. Tremel and G. J. Snyder, Energy Environ. Sci., 2012, 9121-9128.
- 21 E. S. Toberer, A. Zevalkink, N. Crisosto and J. G. Snyder, Adv. Funct. Mater., 2010, 4375-4380.
- 22 M. P. Nagu, Ph.D. thesis, The Technical University of Darmstadt, 2014.
- 23 S. M. Kauzlarich, C. L. Condron, J. K. Wassei, T. Ikeda and J. G. Snyder, J. Solid State Chem., 2009, 182, 240-245.
- 24 S. Kim, C. Kim, Y. Hong, T. Onimaru, K. Suekuni, T. Takabatake and M. Jung, J. Mater. Chem. A, 2014, 2, 12311-12316.
- 25 H. Tamaki, K. H. Sato and T. Kanno, Adv. Mater., 2016, 1-6.
- 26 K. Silsby, F. Sui, X. Ma, S. M. Kauzlarich and S. E. Latturner, Chem. Mater., 2015, 27(19), 6708-6716.
- 27 G. Cordier and H. Ochmann, Z. Kristallog., 1991, 308–309.
- 28 U. Aydemir, A. Zevalkink, A. Ormeci, S. Bux and J. G. Snyder, J. Mater. Chem. A, 2016, 4, 1867-1875.
- 29 U. Aydemir, A. Zevalkink, A. Ormeci, G. M. Zachary, S. Bux and J. G. Snyder, Chem. Mater., 2015, 27, 1622-1630.
- 30 Y. Pei, Z. M. Gibbs, A. Gloskovskii, B. Balke, W. G. Zeier and G. J. Snyder, Phys. Rev. B: Condens. Matter Mater. Phys., 1998, 57, 1505-1509.
- 31 B. H. Toby and R. B. Von Dreele, J. Appl. Crystallogr., 2013, 46, 544-549.
- 32 K. A. Borup, J. de Boor, H. Wang, F. Drymiotis, F. Gascoin, X. Shi, L. Chen, M. I. Fedorov, E. Muller, B. B. Iversen and G. J. Snyder, Energy Environ. Sci., 2015, 8, 423-435.
- 33 S. Iwanaga, E. S. Toberer, A. LaLonde and G. J. Snyder, Rev. Sci. Instrum., 2011, 82, 063905.
- 34 G. Kresse and J. Furthmüller, Phys. Rev. B: Condens. Matter Mater. Phys., 1996, 54, 11169-11186.
- 35 P. E. Blöchl, Phys. Rev. B: Condens. Matter Mater. Phys., 1994, 50, 17953-17979.

- 36 P. Gorai, P. Parilla, E. S. Toberer and V. Stevanovic, *Chem. Mater.*, 2015, 27, 6213.
- 37 S. L. Dudarev, G. A. Botton, S. Y. Savrasov, C. J. Humphreys and A. P. Sutton, *Phys. Rev. B: Condens. Matter Mater. Phys.*, 1998, 57, 1505–1509.
- 38 V. Stevanovic, S. Lany, X. Zhang and A. Zunger, *Phys. Rev. B: Condens. Matter Mater. Phys.*, 2012, **85**, 115104 1–12.
- 39 A. Zevalkink, E. S. Toberer, W. G. Zeier, E. Flage-Larsen and G. J. Snyder, *Energy Environ. Sci.*, 2011, 510–518.
- 40 W. G. Zeier, A. Zevalkink, E. Schechtel, W. Tremel and G. J. Snyder, *J. Mater. Chem.*, 2012, 9826–9830.
- 41 A. Zevalkink, G. Pomrehn, Y. Takagiwa, J. Swallow and G. J. Snyder, *ChemSusChem*, 2013, 2316–2321.
- 42 H. Goldsmid and J. Sharp, J. Electron. Mater., 1999, 869-872.
- 43 H. Kim, Z. M. Gibbs, Y. Tang, H. Wang and G. J. Snyder, *APL Mater.*, 2015, 3, 041506.
- 44 E. S. Toberer, A. Zevalkink and J. G. Snyder, *J. Mater. Chem.*, 2011, 15843–15852.